

Dense Molecular Gas In A Young Cluster Around MWC 1080 – Rule Of The Massive Star

Shiya Wang, Leslie W. Looney

Department of Astronomy, University of Illinois, 1002 W. Green St., Urbana, IL 61801

swang9@astro.uiuc.edu, lwl@uiuc.edu

Wolfgang Brandner

Max-Planck-Institut für Astronomie, Heidelberg, Germany

Laird M. Close

Steward Observatory, University of Arizona

ABSTRACT

We present CS $J = 2 \rightarrow 1$, $^{13}\text{CO } J = 1 \rightarrow 0$, and C $^{18}\text{O } J = 1 \rightarrow 0$, observations with the 10-element Berkeley Illinois Maryland Association (BIMA) Array toward the young cluster around the Be star MWC 1080. These observations reveal a biconical outflow cavity with size ~ 0.3 and 0.05 pc for the semimajor and semiminor axis and $\sim 45^\circ$ position angle. These transitions trace the dense gas, which is likely the swept-up gas of the outflow cavity, rather than the remaining natal gas or the outflow gas. The gas is clumpy; thirty-two clumps are identified. The identified clumps are approximately gravitationally bound and consistent with a standard isothermal sphere density, which suggests that they are likely collapsing protostellar cores. The gas kinematics suggests that there exists velocity gradients implying effects from the inclination of the cavity and MWC 1080. The kinematics of dense gas has also been affected by either outflows or stellar winds from MWC 1080, and lower-mass clumps are possibly under stronger effects from MWC 1080 than higher-mass clumps. In addition, low-mass cluster members tend to be formed in the denser and more turbulent cores, compared to isolated low-mass star-forming cores. This results from contributions of nearby forming massive stars, such as outflows or stellar winds. Therefore, we conclude that in clusters like the MWC 1080 system, effects from massive stars dominate the star-forming environment in both the kinematics and dynamics of the natal cloud and the formation of low-mass cluster members. This study provides insights into the effects of MWC 1080 on its natal cloud, and suggests a different low-mass star forming environment in clusters compared to isolated star formation.

Subject headings: ISM: clouds—ISM: jets and outflows—radio lines: ISM— stars: formation—stars: individual (MWC 1080)

1. Introduction

Stars are born deep within molecular clouds. For the last few decades, it has been well established that an isolated solar-like (low-mass) star forms and evolves through the process of active infall and circumstellar accretion of the material provided by the natal cloud, before reaching the main sequence stage (e.g. Shu et al. 1993). At the same time, the forming star also effectively disperses the surrounding molecular gas via outflows and jets (see review, Arce et al. 2007). Molecular outflows have been suggested to be the main sources clearing the circumstellar material around a forming low mass star. Highly collimated CO flows are ubiquitous with low mass protostars of age $< 10^5$ yrs, having velocities of 10-100 km s $^{-1}$ and typical mass loss rates of 10^{-6} M $_{\odot}$ yr $^{-1}$. However, there has been increasing evidence showing that the outflow characteristics, especially the collimation, and even the mechanisms, actually evolve with the low mass protostar (e.g. Tobin et al. 2007). Nevertheless, the star forming environment is dramatically impacted by the evolution of the forming star.

The formation of an intermediate-mass star (3 - 20 M $_{\odot}$) is probably similar to low-mass star formation. For example, the Herbig Ae/Be stars (HAeBes, Herbig 1960) are thought to be the intermediate-mass classical T-Tauri stars (CTTs) (see review, Waters & Waelkens 1998), which are protostars with primordial accretion disks but mostly dispersed infalling envelopes. However, more and more observational evidence suggests that the formation of massive stars, especially with spectral types of early B to O, is not simply a scaled-up version of low-mass star formation (see review, Zinnecker & Yorke 2007). Nevertheless, like a low mass star, gas dispersal is also expected for a HAeBe. Fuente et al. (1998a, 2002) mapped the molecular gas around HAeBes with different evolutionary stages and showed that the material around HAeBes are usually continuously swept out by outflows to form cavities as the HAeBes evolve. This also implies an alternative classification to characterize the evolutionary stage of HAeBes, in addition to the near-infrared scheme (Hillenbrand et al. 1992). Indeed, outflows associated with intermediate mass to massive protostars have started to be identified (e.g. Wu et al. 2005). It is suggested that the outflows of B stars have higher mass loss rates of 10^{-5} to 10^{-3} M $_{\odot}$ yr $^{-1}$ with less collimation (e.g. Wu et al. 2005), compared to outflows from low-mass protostars.

In addition to the formation of isolated stars, more and more studies have started to focus on cluster systems, which are actually the major mode of star formation in the Galaxy (Carpenter 2000; Lada & Lada 2003). For example, Ridge et al. (2003) mapped the dense

gas around young clusters within 1 kpc and also suggested a similar classification of cloud evolution, as seen in HAeBe systems (Fuentes et al. 1998a, 2002). However, as a typical cluster normally contains several intermediate- to high-mass stars surrounded by 10’s to 100’s low-mass stars (e.g. Hillenbrand 1995; Wang & Looney 2007), one would expect that the forming environment of those low-mass cluster members must be dynamically affected by the nearby more massive stars. Is there any difference or modification of gas dispersal processes in clusters, compared to isolated stars– What roles do massive stars play in clusters? On the other hand, how do low-mass cluster members contribute?

In order to investigate the gas dispersal in the cluster environment, we study one of the nearby embedded young clusters around HAeBes, the MWC 1080 system. The MWC 1080 system is a small stellar group embedded within the dark cloud LDN 1238 (Lynds 1962) at 2.2 kpc (Canto et al. 1984; Ábrahám et al. 2000). The most luminous star, MWC 1080 (V628 Cas), has been classified as a B0e star (Cohen & Kuhi 1979), with $20.6 M_{\odot}$, $10^4 L_{\odot}$ (Hillenbrand et al. 1992; Hillenbrand 1995), and a flat optically thick circumstellar disk (Hillenbrand Class I object for Herbig Ae/Be stars). Within 0.2 pc, it is surrounded by at least 15 stars presenting large near infrared excesses (Hillenbrand 1995). Not only infrared excesses, but the discoveries of molecular outflows, a P-Cygni feature in the H α line, and several nearby HH objects, also indicate active accretion and thus the youthfulness of this system (< 1 Myr) (Fuentes et al. 1998a; Finkenzeller & Mundt 1984; Poetzel et al. 1992; Yoshida et al. 1992). Levreault (1988) estimates an outflow age of 2.2×10^5 yrs. Thus, the age of this system is $\sim 0.1 - 1$ Myr. Single-dish maps of CO, ^{13}CO , C ^{18}O , and CS also show that this group is associated with more than $1000 M_{\odot}$ of molecular material within 1 pc (Hillenbrand 1995) and $\sim 10 M_{\odot}$ within 0.08 pc (Fuentes et al. 2002). Judged by the age of MWC 1080, this system is actually young enough to still have molecular gas but also old enough to have shown the influence of MWC 1080– the natal gas is dispersing. Therefore, it provides a valuable system to study the molecular gas evolution and star formation in a cluster environment.

In this paper, we present high spatial- and spectral-resolution data obtained with the BIMA array in the CS(2-1), $^{13}\text{CO}(1-0)$, C $^{18}\text{O}(1-0)$, and 3 mm dust continuum emission toward the MWC 1080 system. BIMA’s high angular resolution can probe the dense gas and dust in this young stellar cluster on spatial scales of 1000’s to 10,000’s of AU. These molecular transitions are typical tracers for dense gas due to their high critical densities ($n \sim 10^4 - 10^6 \text{ cm}^{-3}$), which helps reveal star-forming clumps and further probe the kinematics and physical conditions in the system.

2. Observations

MWC 1080 was observed using the line transitions CS $J = 2 \rightarrow 1$, $^{13}\text{CO } J = 1 \rightarrow 0$, and $\text{C}^{18}\text{O } J = 1 \rightarrow 0$ with the 10-element Berkeley Illinois Maryland Association (BIMA) Array (Welch et al. 1996). The CS $J = 2 \rightarrow 1$ ($\nu = 97.981$ GHz) observations in C and B array configurations were obtained in October and December 2003. The correlator was configured with the line window of a velocity range of 76 km s^{-1} with 0.3 km s^{-1} per channel, and two 600 MHz bands for continuum. The system temperatures during the observations ranged from 150 - 700 K. The $^{13}\text{CO } J = 1 \rightarrow 0$ ($\nu = 110.201$ GHz) and $\text{C}^{18}\text{O } J = 1 \rightarrow 0$ ($\nu = 109.782$ GHz) observations in B and C array configurations were obtained in March and April 2004. The correlator was configured with the line window of a velocity range of 135 km s^{-1} with 1.0 km s^{-1} per channel, and two 150 MHz bands for continuum. The system temperatures during the observations ranged from 230 - 1000 K.

The data were reduced with the MIRIAD package (Sault et al. 1995) and mapped using two array configurations with various u, v weighting schemes to stress structures on spatial scales from $2''$ to $9''$.

We also obtained a continuum submillimeter map of MWC 1080 at $\lambda = 850 \mu\text{m}$ from the archive data of the Submillimeter Common User Bolometer Array (SCUBA) instrument on the James Clerk Maxwell Telescope (JCMT).

3. The Morphology of Dense Gas around MWC 1080

The BIMA interferometry data provide the highest resolution observations to date, revealing the dense gas in this cluster. We have weighted the data to probe the structures with spatial scales of $2''$ - $9''$ for CS, ^{13}CO , and C^{18}O . These sizes correspond to spatial resolutions roughly from 20000 AU down to 4000 AU, which is a good scale of probing low-mass star forming clumps (e.g. Looney et al. 2000).

3.1. The Distribution of Dense Gas

The left portion of Figure 1 plots the velocity-integrated CS contours overlaid on an K'-band adaptive optics observation from the 3.6m CFHT of the core stellar population (Wang et al. in prep., Paper II hereafter). The right portion zooms into the core with this $\sim 0.1''$ resolution K'-band image (Paper II), which illustrates not only the distribution of cluster members but also the morphology of a reflection nebulae with a hourglass structure

at the NW-SE direction (called the hourglass axis). This Hokupa’a 36 (Graves et al. 1998) adaptive-optics near-infrared (JHK’) observation and the photometry of cluster members will be presented in Paper II. The reflected light results from the existence of dense dust whose surface is illuminated by the UV radiation from MWC 1080.

The CS map shows two distinct branches of emission (Figure 1), which we call East and West for the left and right branch, respectively. Figure 1 shows that the distribution of CS emission is clearly aligned with the obscuring and scattering dust seen in the near-infrared map. This suggests the existence of a previous bipolar outflow that cleaned out the natal material along the direction perpendicular to the hourglass axis (the outflow axis), and helped clear the view to the stellar population along this direction. However, the CS emission is only associated with the upper part of the dense dust, revealing only the upper half of the cavity structure; the molecular gas is denser in the upper part than the lower part.

Moreover, the ^{13}CO map also supports the suggestion of bipolar outflows by revealing a nearly complete biconical cavity around MWC 1080 (see Figure 2). Figure 2 plots the velocity-integrated ^{13}CO and C^{18}O contours as well as the $\lambda = 850\ \mu\text{m}$ and $\lambda = 3\ \text{mm}$ dust continuum. The ^{13}CO morphology also gives an lower limit of the estimation for the outflow cavity with ~ 0.3 and $0.05\ \text{pc}$ for the semimajor and semiminor axis and $\sim 45^\circ$ position angle. This is just a lower limit because possible inclination or projection effects have not been taken into account. Fuente et al. (1998a, 2002) investigates the evolution of dense gas dispersal around HAeBes by presenting IRAM single-dish ^{13}CO and CS observations. They propose an evolutionary sequence from stars that are still embedded within dense clumps and associated with bipolar outflows (Type I) to stars that have dispersed their natal clouds and formed cavities (Type III). MWC 1080 is shown to be their Type II system. Our high spatial-resolution observations further show that although this system is still young, age $< 1\ \text{Myr}$, the bipolar outflows in the MWC 1080 system has already constructed a small cavity, which is revealed for the first time. The size of this cavity is much smaller, compared to the cavities seen in older systems, such as HD 200775, a HAeBe with age of $8\ \text{Myr}$ and a cavity of size $\sim 1.5\ \text{pc} \times 0.8\ \text{pc}$ (Fuente et al. 1998b). This might suggest that the bipolar outflow activity around MWC 1080 is still an ongoing process that will form a larger cavity.

From Figure 2, the dust morphology at $\lambda = 850\ \mu\text{m}$ is similar to the morphology of dense gas, which infers that the dense gas traces well the dust around MWC 1080. The high resolution of the $\lambda = 3\ \text{mm}$ continuum BIMA map reveals five dust clumps, which are consistent with dense gas distribution as well.

In addition to the morphology, more information, such as the clumpiness, kinematics and physical conditions inside this system, can be further investigated by extracting the

mass and velocity distribution of dense gas. Studying the clumpiness of a molecular cloud is essential as it is usually closely related to the fragmentation and collapsing of molecular cores inside the cloud, which provides valuable insights to the ongoing star-forming activities in the system. On the other hand, the kinematics of gas and physical conditions reveal the natal environment where stars were born. As CS traces a denser region than ^{13}CO , we mainly use CS to examine the clumpiness of dense gas, and use both CS and ^{13}CO to reveal the kinematics and physical conditions in this system.

3.2. Clumpiness of Dense Gas

Clumpiness is always observed in molecular clouds. This is not surprising as a star forms through collapsing the natal cloud after reaching certain collapsing criteria. Therefore, local fragmentation and further clumping are naturally two typical characteristics in star forming clouds. With the ability of interferometric observations to peer into dense layers of the molecular cloud, we can study how clumpy the dense gas is and its clump size, compared to those cores forming isolated stars.

A clump is defined as a local density enhancement, which results in a flux density enhancement observationally. A molecular cloud without clumpy structures will not show multiple local emission peaks in its map, no matter how small the probing scale, or beam size. On the other hand, if clumps exist in a molecular cloud, the number of local emission peaks will increase with decreasing scale, until all clumps have been picked up or some clumps are too weak to be detected. Therefore, high resolution maps are essential to distinguish clumpy structures in the molecular clouds.

Figure 3 plots the CS contours at four different mapping scales with $8''$, $4''$, $3''$, and $2''$ beams. Fuente et al. (1998a) published the IRAM single-dish molecular line and continuum data of MWC 1080 and showed one emission peak near MWC 1080 in their ^{13}CO (1-0) and CS (3-2) maps with a $24''$ and $16''$ beam respectively, and two emission peaks around MWC 1080 at the 1.3 mm continuum map with a $\sim 11''$ beam. By comparing these maps, more and more clumps are seen from their maps to our Figure 3, and from Figure 3(a) to 3(c). This indicates that the dense gas around MWC 1080 is not a single big cloud centered on MWC 1080 but rather consists of small clumps, with clump sizes down to $\sim 3''$ (6600 AU). However, there is not much difference in the clumpy structures between Figure 3(c) to Figure 3(d), which suggests that the u , v weights used in Figure 3(d) are less suitable to the majority of the dense gas. The reason is that the dense gas in Figure 3(d) is resolved out with the interferometer. Therefore, in this paper, we will use Figure 3(c) to further identify clumps and study their physical properties.

The main purpose of identifying clumps is to obtain individual star-forming building blocks that are capable of forming one or multiple low-mass protostars, in order to investigate their physical condition, such as mass, velocity dispersion, spectral feature, etc., in each system. In order to identify clumps, we basically adapt the idea of the *Clumpfind* method (Williams et al. 1994) to: (1) select local peaks with fluxes above 3σ in the velocity-integrated CS map (Figure 3(c)), (2) trace down to the half-maximum (HM) flux level of contours, which determines the sizes of clumps by fitting an ellipse, (3) assign the contour to the nearest peak once this contour is shared by more than one peak, (4) extract the spectrum and mass of each clump within the clump size, and (5) fit the extracted spectra with Gaussian to obtain the peak flux, peak velocity, and line width (FWHM). This is different from directly using three-dimension cubes because it can avoid some specific star forming features, such as a P-Cyg profile being mis-separated into two clumps.

Table 1 lists parameters of 32 identified clumps, including coordinates, sizes, and integrated fluxes (I_t). The a_o , b_o , PA_o , a , b , and PA are the observed and deconvolved sizes, including the major axis (a), minor axis (b), and the position angle (PA), respectively. We directly use the beam size as the upper limit of clumps with deconvolved sizes smaller than the beam size. The R_{eq} is $\sqrt{ab}/2$, the equivalent size assuming a spherical clump. The sizes of identified clumps range from ~ 4000 AU to 10000 AU. This is generally consistent with a typical system forming a single isolated low mass star (e.g., ~ 5000 AU, Looney et al. 2003).

Moreover, the eccentricity of clumps, ε , derived by a and b , can be used to characterize the clump shape. From the derived values of projected eccentricity, we can see that not all clumps have circular morphology, especially for those closer to MWC 1080, which show somewhat elongated structures with larger eccentricities. In order to examine the spatial distribution of clump eccentricity, we plot the eccentricity vs. the distance to MWC 1080 (Figure 4(a)) and to the outflow axis (Figure 4(b)) for those resolved clumps. This plot shows that clumps closer to both the outflow axis and MWC 1080 tend to have larger projected eccentricities. This implies that clumps are more elongated when located closer to MWC 1080. This also suggests possible effects from outflows on the morphology of dense gas, especially modifying the shape of clumps.

4. The Kinematics of Dense Gas

We study the kinematics of the dense gas by investigating its velocity distribution. The spectral resolution of CS, ^{13}CO , and C^{18}O , observations are 0.299 , 1.034 , and 1.034 km s^{-1} , respectively, with V_{LSR} at 29.3 km s^{-1} (Hillenbrand 1995). As can be seen in Figure 1 and 2, CS and ^{13}CO trace more gas than C^{18}O does and CS traces gas with higher density than

the other two transitions. We will use both CS and ^{13}CO to display the overall velocity distribution of dense gas and specifically use CS to examine the kinematics of identified clumps.

4.1. Overall Velocity Distribution

Figure 5 displays the integrated spectra of CS, ^{13}CO , and C^{18}O emission, and Figure 6 shows the integrated CS spectra of East and West. From Figure 5, we can see that all CS and C^{18}O and most ^{13}CO emission are blue-shifted, compared to the V_{LSR} . In addition, a double-peaked feature is seen in the integrated spectra of ^{13}CO and CS. Figure 6 shows that the spectrum of East is single-peaked with a broad linewidth, while West contains two components. Table 2 lists the Gaussian-fitted parameters of these integrated spectra. From all integrated spectra, a large velocity gradient of the dense gas is seen throughout the whole system; the separation of peak velocity between two components in West is as large as 3.3 km s^{-1} .

In order to reveal the velocity distribution and investigate the double-peaked feature, Figure 7 shows the position-velocity (PV) diagrams for East and West from CS and ^{13}CO maps. This is made by applying two cuts from south to north toward both portions, as the dense gas of two portions are elongated along the outflow axis. Interestingly, it shows that two components seen in the integrated CS spectrum of West are also spatially distinguishable—the blue and red component in the spectrum are related to the northern and southern part of the dense gas in West, respectively. Canto et al. (1984) also detected a double-peak feature on the spectrum of dense gas around MWC 1080, but explained it as the results from self-absorption due to poor spatial resolution. Our high-resolution interferometric data shows that this double-peaked feature actually comes from two sets of gas with different velocities. In addition to West, Figure 7 also shows that there is a systematic velocity gradient in East from -35 km s^{-1} (bluer, south) to -30 km s^{-1} (redder, north), especially seen in the ^{13}CO map. This gradient may result from an inclination of the outflow cavity, as the direction of the gradient is along the outflow axis.

Not only is there a velocity variation along the outflow axis, there is also a velocity gradient along the hourglass axis, which is perpendicular to the outflow axis. Figure 8 is the PV diagrams of the CS map with three cuts perpendicular to the outflow axis and moving away from MWC 1080. This also shows that the velocity dispersion along the farther cut is larger than that along the closer cut from MWC 1080. This is contrary to the idea that outflows or stellar winds from MWC 1080 contribute to the nonthermal motion, thus increase the velocity dispersion, of gas closer to MWC 1080.

4.2. Spectra of Identified CS Clumps

Figure 9 displays example spectra of our identified clumps. Table 3 lists Gaussian-fitted parameters of the clumps that can be fitted with Gaussian. A few of them show P-Cyg-like absorption; several of them contain two peaks, which might come from either self-absorption or a secondary component (another clump along the line of sight).

5. Estimating the Column Density and Mass of Dense Gas

Several methods have been used to estimate the column density from molecular emission, such as a direct estimation from individual transitions (Miao et al. 1995; Friedel 2005), the Large Velocity Gradient approximation (LVG, Goldreich & Kwan 1974), rotational temperature diagrams (RTD, e.g., Friedel 2005), etc. Since we only have individual transitions for each molecular species, we use a simple LTE method for all column density estimated in this paper, and also use the LVG models for those CS clumps with fitted spectra for comparison.

5.1. LTE Approximation

By assuming LTE with an excitation temperature T_{ex} , small opacity and negligible background continuum contribution, the total column density from a single transition using an array can be derived by (e.g., Miao et al. 1995),

$$N = \frac{2.04IC_\tau}{\theta_a\theta_bS\mu^2\nu^3}Qe^{\frac{E_u}{T_{ex}}} \times 10^{20} \text{ cm}^{-2}. \quad (1)$$

I is the total integrated intensity in $\text{Jy beam}^{-1} \text{ km s}^{-1}$, θ_a and θ_b are the FWHM sizes of beams in arcseconds, S , μ^2 , ν , Q , and E_u are the line strength, dipole moment in Debyes, line frequency in GHz, partition function, and energy in K of the upper state, respectively (Table 4). We use the deconvolved source sizes, a and b , as θ_a and θ_b here. C_τ is the opacity correction factor (Goldsmith & Langer 1999),

$$C_\tau = \frac{\tau}{1 - e^{-\tau}}.$$

The optical depth, τ , can be derived by (Rohlfs & Wilson 2000),

$$\tau = -\ln\left[1 - \frac{T_{MB}}{J(T_{ex}) - J(2.73)}\right],$$

where T_{MB} is the main beam brightness from observations and $J(T)$ is given by $\frac{h\mu}{k} \frac{1}{e^{h\mu/kT}-1}$. Table 1 lists some of these parameters for CS(2-1), $^{13}\text{CO}(1-0)$, and $\text{C}^{18}\text{O}(1-0)$ (Rohlfs & Wilson 2000).

With estimated column density, mass can be obtained by assuming the abundance ratio to H_2 , X_{CS} , $X_{^{13}\text{CO}}$, and $X_{\text{C}^{18}\text{O}} = 10^{-9}$, 1.26×10^6 , and 1.7×10^{-7} , respectively (Rohlfs & Wilson 2000). An excitation temperature, $T_{ex} = 20$ K, is assumed, as a medium value often seen in dense cores forming massive stars (see review, Zinnecker & Yorke 2007). Therefore, the mass can be derived by

$$M = \mu m_H \frac{N}{X} (1.133abD^2), \quad (2)$$

where $\mu = 2.33$ is the mean molecular weight, m_H is the mass of a hydrogen atom, and D is the distance ($= 2.2$ kpc for MWC 1080; Canto et al. 1984; Ábrahám et al. 2000).

The estimated CS column densities and masses for CS clumps are listed in Table 5, labeled as M_{LTE} , along with the estimated optical depth. The masses of these clumps range from $\sim 1 - 10 M_\odot$, with mean optical depth τ less than 1. We also estimate the maximum optical depth based on the peak emission of the CS map, which gives optical depth ~ 1.2 in this system.

Using the same assumptions and eq. (1) and (2), the total masses of dense gas are also calculated. There are ~ 800 , 1000 , and $900 M_\odot$ for CS, ^{13}CO , and C^{18}O , respectively, within the area of 0.7 pc radius from the MWC 1080.

5.2. LVG Model

Another method, that is frequently used especially for optical thick lines, is the Large Velocity Gradient (LVG) approximation (Goldreich & Kwan 1974). This is a radiative transfer model that takes optical depths into accounts for photon transport. It basically assumes a cloud with a systematic velocity gradient with velocity increasing away from the cloud center, so that a local treatment for photon transport can be approximated. We also estimate column densities and masses of CS clumps based on the LVG model, in order to compare to the previous LTE calculation. We only apply LVG for those 14 CS clumps with well fitted spectral information from Table 3.

We use the *lvg* task in MIRIAD to generate grids of the LVG model with kinetic temperatures of $10 - 30$ K, number densities of $10^4 - 10^8 \text{ cm}^{-3}$, and column densities of $10^{13} - 10^{15} \text{ cm}^{-2}$. By using these grids to fit the observed brightness temperature, a range of CS column

density can be found that can produce the observed emission. We further narrow the obtained range of CS column density by assuming the optical depth $\tau \lesssim 2$. As there is a lack of observations of NH_3 to further constraint the kinetic temperature, we simply use the range of 10 - 30 K, which is typically used for both low-mass and massive star forming regions. The derived column densities and masses of CS clumps are listed in the Table 5.

We also compare the estimation of M_{LTE} and M_{LVG} for these clumps. All clumps, except clumps A2 and A4, show a roughly good agreement between the derived M_{LTE} and M_{LVG} . This consistency suggests that most CS clumps are under good LTE approximation with small opacity. Clumps A2 and A4 have the brightest peak emission. The reason why the LVG model gives much larger column density than the LTE approximation is that there is either a larger opacity or a higher temperature inside these two clumps. Large opacity will give a larger column density in the LTE approximation; while higher temperature than 30 K will allow smaller column density in the LVG model to produce lines with such strong intensity. Both are reasonable explanations, especially the temperature in these two clumps is likely higher than usual, as they are located very close to the source of strong UV radiation, MWC 1080. In this paper, we will use the M_{LTE} for further discussion.

5.3. Virial Mass

With the estimated masses and the velocity dispersion of clumps, we can further study the virial condition inside each clump by comparing clump mass with the virial mass, M_{vir} . M_{vir} is the mass when the system is in virial equilibrium, when the time average over the kinetic energy is equal to half of the potential energy. In this situation, the system is gravitationally bound.

We assume a spherical symmetric clump with total mass M , radius R , and a density profile, $\rho(r) = \rho_0 r^{-\alpha}$, where ρ_0 is the central density and r is the radial distance from the clump center. Therefore,

$$M_{vir} = \frac{5 - 2\alpha}{3 - \alpha} \frac{3R}{G} \frac{\Delta V^2}{8 \ln 2}, \quad (3)$$

where $\alpha \neq 3$. Either uniform density or isothermal condition is often assumed while deriving the virial mass of a cloud. In these two cases,

$$M_{vir} = \frac{5}{3} \frac{3R}{G} \frac{\Delta V^2}{8 \ln 2} \quad (4)$$

for uniform density, and,

$$M_{vir} = \frac{3R}{G} \frac{\Delta V^2}{8 \ln 2} \quad (5)$$

for the isothermal cloud with density $\rho(r) = \rho_0 r^{-2}$.

In order to understand the density profile in our system, we investigate the relation between the total mass and size of CS clumps, by plotting M_{LTE} and R_{eq} (Figure 10), as used in Saito et al. (2006). We obtain a linear relation between these parameters via least-square fittings,

$$\log M_{LTE}(M_{\odot}) = (0.87 \pm 0.32) \log R_{eq}(pc) + (1.82 \pm 0.67), \quad (6)$$

with $\chi_r^2 = 1.35$. This assumes that all clumps in this system around MWC 1080 have the same density structure. Since $\rho(r) = \rho_0 r^{-\alpha}$, which gives $M = \frac{4\pi\rho_0}{3-\alpha} R^{3-\alpha}$, then $\rho_0 = 4.57 \pm 1.69 M_{\odot} \text{ pc}^{-3}$ and $\alpha = 2.13 \pm 0.32$ are obtained. Therefore, in our case

$$M_{vir} \sim \frac{3R \Delta V^2}{G \ln 2}, \quad (7)$$

shows that our systems are consistent with a standard isothermal sphere density (Shu 1977).

Given R_{eq} and FWHM from Table 1 and 3 as R and ΔV^2 , M_{vir} is calculated and listed in Table 5. M_{vir} ranges from $\sim 1 - 10 M_{\odot}$. By comparing M_{vir} with M_{LTE} , we find that the M_{vir} is $\sim 0.4 - 2$ times the M_{LTE} , except A8, C1, and C5, the farthest three clumps away from MWC 1080, which are 2 - 4 times larger than M_{LTE} . In general, we can conclude that the virial mass is similar to the clump mass, as the mass estimation usually has an uncertainty to an order of 2. This is similar to low-mass star forming cores, rather than massive cores (e.g., Saito et al. 2006).

6. Discussion

This paper presents high resolution data for dense gas in the cluster environment around the HAeBe star MWC 1080. The CS transition is especially used to peer into the dense core region. Freeze-out depletion of CS or CO onto dust grains would affect our results. However, molecular depletion mostly occurs in colder cores. For example, CS and CO are often seen to freeze-out onto dust grains in starless cores, which have lower average temperatures, ~ 10 K (see review, di Francesco et al. 2007).

With high resolution, the importance of this study is being able to reveal the physical conditions and examine the sub-structures (i.e. clumps, that may be forming single low-mass cluster members) within this cluster-forming cloud, and distinguish the effects of MWC 1080 and its outflows from the initial cloud environment. We will focus on discussing the effects from MWC 1080 on its natal cloud by characterizing the dense gas, its dispersal history, and star-forming clumps in this cluster. To best study star formation in cluster environments

would require a large sample of objects like MWC 1080; however, these data still provide valuable insights into such systems.

6.1. Gas Removal in Clusters

Outflows are the primary sources to remove the natal material during the formation of stars, in addition to stellar winds and stellar radiation in the core of starburst clusters. However, the gas removal process via outflows in clusters has not been clearly characterized. As there are both high-mass and low-mass members forming in a cluster, the gas removal process might be different from that in a single star forming system. Especially, does the most massive star still dominate the outflows that results in similar gas removal processes as seen from an isolated star? What is the role of low-mass cluster members in the strength and collimation of outflows?

In fact, the existence of a bipolar outflow in this cluster around MWC 1080 has been suggested based on its blue and red components on CO spectra in previous single-dish studies (e.g., Canto et al. 1984; Yoshida et al. 1991). However, due to poor angular resolution of single-dish observations, the outflow properties, such as the direction of the outflow axis, have not been well characterized. From our data, a biconical cavity is distinctly revealed around the most massive star in this system, MWC 1080, suggesting that the bipolar outflow has been dominated by MWC 1080. This also implies evidence of the gas removal by outflows in clusters. With the observed outflow cavity, the outflow axis is also clearly defined to have a PA of 45 degree.

Our data also show that this outflow cavity has a size of 0.3×0.05 pc. This roughly gives an opening angle of 20 degree and a collimation factor of 3. This also means that the outflow activity has begun and formed a small cavity at the age < 1 Myrs for a HAeBe star like MWC 1080. However, gas removal via outflows is still an ongoing process in this system, as a larger outflow cavity has been seen in a similar but older system (HD 200775, 8 Myrs, Fuente et al. 1998b). A future ^{12}CO high resolution observation will be helpful to confirm the ongoing outflow activity in this system, as ^{12}CO can trace low density outflow gas. Assuming a homogeneous mass distribution of gas in the initial natal cloud and an initial mass density the same as the remaining gas, we can estimate that there was $\sim 1000 M_{\odot}$ of gas in the cavity before outflows removed it. Therefore, an outflow mass loss rate $> 10^{-3} M_{\odot}/\text{yr}$ is required to form this cavity, either assuming a outflow age of ~ 0.2 Myrs (Levreault 1988) or an age < 1 Myrs (Fuente et al. 1998a). This value is higher than the typical mass loss rate of outflows from a single OB star ($10^{-3} - 10^{-4} M_{\odot}/\text{yr}$). In fact, previous CO observations, which trace outflow gas at larger scale than this study, have estimated an outflow mass loss rate of \sim

$10^{-4} \text{ M}_{\odot}/\text{yr}$ (e.g. Yoshida et al. 1991; Canto et al. 1984; Levreault 1988). One explanation of possible higher mass loss rate for CS gas is that the outflows from other cluster members are strong enough to strengthen the overall effects, but not enough to change the outflow direction, at the scale of our study. Another possibility is that the remaining gas does not just include the natal material but also the swept-up gas by outflows, so the mass loss rate is overestimated.

In order to clarify whether the observed dense gas is the remaining gas from the initial cluster-forming cloud or the swept-up gas by outflows, we further inspect the possible non-thermal contribution from outflows in dense gas next.

6.2. Non-thermal Contributions in Dense Gas

Molecular clouds, except for single star-forming prestellar cores, are generally observed to have broader linewidths than those caused by the thermal motion from their thermal temperatures. This is suggested to be resulting from the presence of turbulence (see review by Mac Low & Klessen 2004). Is this also true for single star-forming clumps in a cluster around an intermediate- to high-mass star, like the MWC 1080 system? What is the role of the cluster environment in the kinematics of dense gas and clumps within one cluster-forming cloud?

Our data show that the linewidth of clumps range from 0.85 to 2.48 km s^{-1} , which is much larger than 0.63 km s^{-1} , the linewidth of thermal broadening at 20 K . If only thermal motion contributes to the linewidth, the kinematic temperatures of these clumps would range from $36 - 310 \text{ K}$. This is unlikely, except for those clumps very close to MWC 1080, which heats its surroundings via UV radiation. Therefore, our results suggest that most gas in this system has a non-thermal contribution to their kinetic motions. However, what contributes to these non-thermal motions? Initial turbulence, outflows from forming stars, and stellar winds from massive stars are possible candidates.

Initial turbulence is the general non-thermal random motion caused by turbulence in the molecular cloud before forming stars. Larson (1979, 1981) found the linewidth-size relation for molecular clouds with different scales. This relation indicates that there is a power-law relation between the velocity dispersion of molecular clouds and cloud size. Caselli & Myers (1995) further suggested that the non-thermal linewidth-size relation follows different power-law trends for low-mass and massive cores. In other words, non-thermal motion still dominates at small scales for massive clumps, while low-mass clumps show only thermal motions at these scales. Nevertheless, there exist non-thermal components in the

kinematics of molecular clouds, which provides the initial turbulence. Based on our data, we roughly estimate that the radius of this cluster-forming cloud is ~ 0.7 pc. This gives an estimation for the initial turbulence with linewidth of $\sim 1 \text{ km s}^{-1}$ in our system, assuming the linewidth-size relation from Larson (1981). This value is smaller than the linewidth from our integrated spectra (Table 3), which implies that the initial turbulence may not be the only contributor to the non-thermal motion in this system.

In order to confirm more carefully whether there are extra contributors to broaden the linewidth of clumps, we plot the linewidth-size relation for identified clumps in Figure 11, compared to Caselli & Myers (1995). Caselli & Myers (1995) shows the nonthermal linewidth-size relations for massive and low-mass cores. Therefore, in this figure, we add the thermal components to their relations with thermal temperature of 18 K and 10 K for massive (solid line) and low-mass (dashed line) cores, respectively, as assumed in Caselli & Myers (1995). The dotted line indicates the thermal motion of 20 K, which is well below the linewidths of all clumps. It also shows that there is either a flat relation or no correlation between the linewidth and the clump size. When using the relation from Caselli & Myers (1995) as expected initial turbulence contribution, this figure suggests that extra contributions dominate over the initial turbulence and affect more the smaller clumps. Not only the relation, but the linewidth values of identified clumps are also overall larger than those in Caselli & Myers (1995). In addition, Figure 11 also plots the relation between the linewidth and the LTE mass of clumps, compared to the result shown in Larson (1981). It shows that the low-mass clumps seem to deviate more from Larson’s relation. This indicates that the lower-mass clumps are possibly affected more, which implies that the extra contributor to the non-thermal motions may come from a common source outside these clumps, instead of heated contribution from embedded forming stars inside individual clumps.

Both outflows or stellar winds can contribute to the observed non-thermal components of linewidth. From the Figure 11, those extra contributors need to broaden the linewidth by $\sim 1\text{-}1.5 \text{ km s}^{-1}$. Furthermore, Figure 12 plots the relations for the linewidth and mass vs. the distance to MWC 1080. From the linewidth-distance relation, no correlation is shown. As outflows or stellar winds from MWC 1080 are possible contributors to the non-thermal motions of natal gas, the affected linewidth are expected to be broader for clumps closer to MWC 1080. Therefore, this plot possibly suggests that there is less initial turbulence deep inside the core region of this cluster-forming cloud. Besides, it is shown in the linewidth-mass relation that more massive clumps form closer to MWC 1080, which is or is close to the center of this cluster-forming cloud.

In short, the kinematics of dense gas in this cluster has been effectively modified by outputs from forming stars, such as outflows and stellar winds, instead of still being sustained

by the initial turbulence. This further suggests that the observed hourglass dense gas is much more likely to be swept-up gas.

6.3. Implications from the Dense Gas Morphology

Who forms first in a cluster– massive or low-mass stars? This has been an fundamental but difficult question in the study of cluster formation, because highly embedded nature of protoclusters, where massive star forms, have prevented us from catching the earliest stage of the formation of low-mass cluster members. However, clarifying this question is essential as it helps understand the star forming environment in clusters and after all most low-mass stars actually form in such cluster environments. This also plays an important role in studying massive star formation as massive stars often form in clusters along with many low-mass stars.

Our results have suggested that the observed molecular lines most likely trace the swept-up gas on the outflow cavity wall, instead of outflows or remaining gas with initial density. The kinematics of the swept-up gas has also been effectively modified by outflows or stellar winds from MWC 1080. The biconical cavity implies a domination of MWC 1080 and also eliminates the contribution of other cluster members. In addition, Paper II also presents that there are ~ 50 low-mass stars within 0.3 pc radius around MWC 1080. Most of these stars are located inside the outflow cavity (also see Figure 1 and 2).

These results may imply that it is unlikely to form low-mass cluster members after MWC 1080 in this system. If low-mass cluster members form after MWC 1080 does, then the gas dispersal from MWC 1080 should eliminate the formation of low-mass cluster members along the outflow direction. Hence, the stellar density in the cavity should have been lower than observed, if these low-mass stars formed after MWC 1080.

However, one puzzle remains about the morphology– why does CS emission only trace the upper half of the outflow cavity? In other words, why is the gas in the upper part denser than the lower part? One explanation is an inhomogeneous distribution of initial natal gas; the gas is just denser in the upper side than the lower side. Another explanation is that this is due to the inclination of outflow cavity, as all CS emission is blue-shifted and a gradient has been seen in Figure 8. The asymmetry of the opening angle between both sides from the ^{13}CO map also may also result from the inclination.

6.4. Clumpiness of Dense Gas vs. Gas Dispersal History

As stars form, they disperse their natal material, so studying the morphology of molecular gas around newly forming stars has been very helpful to distinguish stars with different evolutionary stages (e.g., Fuente et al. 1998a, 2002). A star-forming cloud typically evolves from compact dense gas centered on the star, to dense gas with bipolar outflows, then finally to a cavity with little gas left. However, not only the natal molecular cloud, but the clumpiness of dense gas in the cloud may also be actively affected by the dispersal processes from the forming star. Therefore, the clumpiness of dense gas might be able to provide an alternative point of view to describe the evolutionary stages of star formation.

The clumpiness of dense gas can be defined as: (1) the fraction of mass inside clumps to total mass; or (2) the number density of clumps— number of clumps per projected area. The first definition is determined by the intrinsic star forming efficiency in the cloud and the degree of gas dispersal; the second definition is determined by the intrinsic fragmentation in the cloud and the degree of gas dispersal. Both definitions depend on the gas dispersal history because the mass inside clumps decreases and the clumps disappear as stars form. Therefore, the clumpiness can actually be used to trace the evolutionary stages of the forming stars, assuming the same initial conditions in the cloud and similar star forming processes. This assumption is valid if we simply apply and compare the clumpiness to similar systems, for example, to clusters around HAeBes like MWC 1080. However, we have to keep in mind that the cloud’s initial conditions may dominate the clumpiness, as different star or cluster forming mechanisms could result in various initial cloud conditions.

In this paper, we will only use the second definition to discuss the clumpiness. This is because the true mass inside clumps can not be fully obtained and the first definition will be biased with the dependence of mapping scales, due to the limitation of interferometry. Looney et al. (2006) identifies 16 clumps from another cluster around HAeBes including BD +40° 4124. Using the second definition, we find that the clumpiness in the BD +40° 4124 system is ~ 1.6 times larger than that in the MWC 1080 system. This suggests that the dense gas seen in the BD +40° 4124 system is at a younger stage than that in the MWC 1080 system.

From the infrared SED classification (Hillenbrand et al. 1992), BD +40° 4124 and MWC 1080 are both classified as Group I objects, which have rising SED slopes. From the gas dispersal history (Fuente et al. 1998a, 2002), they are both associated with compact dense gas, which suggests a similar evolutionary stage. In addition, from the CS maps using high resolution interferometric observations (Figure 1 in Looney et al. 2006 for BD 40° +4124 and Figure 5(b) here), both systems show that the CS distributions are actually offset from the most massive stars— still at a similar evolutionary stage. Looney et al. (2006) show that the

dense gas is around other younger stars, not BD+40° 4124. The clumpiness discussed here suggests the youthfulness of dense gas in the BD +40° 4124 system and also shows that the dense gas in the MWC 1080 is dominated by MWC 1080, unlike the BD +40° 4124 system. Indeed, the clumpiness provides an alternative point of view to examine the evolutionary stages of young stars, other than the morphology of dense gas or the SEDs of young stars.

6.5. Dynamics of Clumps

Our data have shown that the mass of identified clumps ranges from ~ 0.5 to $10 M_{\odot}$, capable of forming low-mass stars, with equivalent radius from 0.01 to 0.04 pc. These clumps are, in general, more massive than protostellar cores with similar sizes. This suggests that clumps formed in a cluster environment tend to have higher densities, which is also shown in Saito et al. (2006).

In addition, all clumps are estimated to have masses similar to the virial masses, which suggests that they are close to being in virial equilibrium. Figure 13 compares the LTE mass and LVG mass vs. virial mass for all clumps. This figure shows that most clumps have masses within 2 times of their virial masses, which means that they are self-gravitational bound systems. This is usually seen in low-mass cores; but it is different from turbulent cores in massive star-forming regions (Saito et al. 2006), showing larger virial masses than LTE masses. This may be due to the external gas pressure helping support the turbulence (Saito et al. 2006). However, according to their Table 4, cores with LTE masses $< 10 M_{\odot}$ are actually close to their virial masses, which is consistent with our results.

Nevertheless, our clumps in the MWC 1080 system are self-gravitationally bound, similar to low-mass star-forming cores, but have a higher density like massive cores. This is not surprising as more mass is needed to bound clumps in order to overcome the non-thermal motions, which are contributed not only by initial turbulence but also inputs from massive stars, such as outflows and stellar winds. This does not necessary mean that they will form massive stars eventually, because they will experience stronger external gas removal, such as outflows from nearby massive stars, than those isolated star-forming cores. In fact, we can simply assume that the identified clumps are possible precursors of those NIR-identified low-mass cluster members (Paper II), that are revealed just because their surrounding gas is strongly dispersed by outflows from MWC 1080. This means that these clumps will indeed be likely forming low-mass stars.

In addition, from Sec. 5.3, we derive a density profile for the identified clumps, $\rho(r) \sim r^{-2.13 \pm 0.32}$. This is consistent with Saito et al. (2006), which shows a density profile of ρ

$\sim r^{-1.9}$ for cores in massive star-forming regions. Our results show that clumps in our system are consistent with the density profile of many protostellar collapse models (e.g., Tassis & Mouschovias 2005). Therefore, along with the fact that these clumps are gravitationally bound, the $\sim r^{-2}$ profile from our data suggest that these clumps are likely collapsing protostellar cores.

We simply conclude that low-mass stars in the cluster environment like the MWC 1080 system tend to be formed in dense and turbulent cores, which are different from isolated low-mass star-forming cores but similar to massive cores. However, gas dispersal contribution from the massive cluster member prevents these dense and turbulent cores from forming massive stars, instead forming low-mass stars, which are also revealed earlier than isolated low-mass stars are. This indicates that massive stars in clusters do have effects on the formation of their low-mass cluster members— both help and hinder.

7. Conclusions

We present BIMA CS(2-1), $^{13}\text{CO}(1-0)$, $\text{C}^{18}\text{O}(1-0)$, and 3mm continuum observations toward the young cluster around MWC 1080, which is a $\sim 20 M_{\odot}$ massive star with the age < 1 Myr. We summarize our results as follows.

- A biconical cavity, with size of 0.3×0.05 pc and $\sim 45^{\circ}$ position angle, is revealed, which suggests the presence of bipolar outflows. The outflows are dominated by the MWC 1080, and effectively modifying the morphology of clumps.
- The observed molecular lines trace the swept-up gas on the cavity wall, instead of the initial natal material or the outflow gas.
- The observed gas is clumpy; 32 CS clumps are identified with mass ranging from 1 - $10 M_{\odot}$. All clumps are approximated under the virial equilibrium, which suggests that they are gravitationally bound, and isothermal. This suggests that they are likely collapsing protostellar cores.
- The gas is mostly blue-shifted. We identify two distinct clouds with different velocities that were thought to be self-absorption. Velocity gradients have also been revealed suggesting an inclination of the outflow cavity and some effects from MWC 1080.
- Both overall gas and clumps show broader linewidths than thermal motion at 20 K. The non-thermal component is possibly contributed by outputs from MWC 1080, such as outflow and stellar wind, in addition to the initial turbulence often seen in the

molecular cloud. This suggests that the kinematics of dense gas has been affected by either outflow or stellar wind from MWC 1080; lower-mass clumps are more strongly effected from MWC 1080 than higher-mass clumps.

- Clumps in clusters have, in general, higher densities than isolated star-forming cores. This results from non-thermal contributions, such as outflows or stellar winds, from nearby forming massive star or stars. However, low-mass stars can still be forming from these clumps, because of the increased gas dispersal from MWC 1080. Therefore, low-mass cluster members tend to be formed in dense and turbulent cores, which are different from isolated low-mass star-forming cores.

In summary, our results show that in the cluster like MWC 1080 system, effects from the massive star dominate the star-forming environment in the cluster, in both kinematics and dynamics of the natal cloud and the formation of low-mass cluster members. However, more studies in similar systems like the MWC 1080 cluster are needed in the future, in order to systematically confirm the effects from massive stars.

We thank Dr. Mordecai-Mark Mac Low for valuable suggestions. We thank Dr. Murad Hamidouche for assistant with the SCUBA data reduction. S.W. and L.W.L. acknowledge support from the Laboratory for Astronomical Imaging at the University of Illinois, NSF AST 0228953. The James Clerk Maxwell Telescope is operated by the Joint Astronomy Centre on behalf of the Science and Technology Facilities Council of the United Kingdom, the Netherlands Organisation for Scientific Research, and the National Research Council of Canada. The JCMT Archive project is a collaboration between the Canadian Astronomy Data Centre (CADC), Victoria and the James Clerk Maxwell Telescope (JCMT), Hilo.

REFERENCES

- Ábrahám, P., Leinert, C., Burkert, A., Henning, T., & Lemke, D. 2000, *A&A*, 354, 965
- Arce, H. G., Shepherd, D., Gueth, F., Lee, C.-F., Bachiller, R., Rosen, A., & Beuther, H. 2007, *Protostars and Planets V*, 245
- Canto, J., Rodriguez, L. F., Calvet, N., & Levreault, R. M. 1984, *ApJ*, 282, 631
- Carpenter, J. M. 2000, *AJ*, 120, 3139
- Caselli, P. & Myers, P. C. 1995, *ApJ*, 446, 665

- Cohen, M. & Kuhi, L. V. 1979, *ApJS*, 41, 743
- di Francesco, J., Evans, II, N. J., Caselli, P., Myers, P. C., Shirley, Y., Aikawa, Y., & Tafalla, M. 2007, in *Protostars and Planets V*, ed. B. Reipurth, D. Jewitt, & K. Keil, 17–32
- Finkenzeller, U. & Mundt, R. 1984, *A&AS*, 55, 109
- Friedel, D. N. 2005, PhD thesis, University of Illinois at Urbana-Champaign, United States – Illinois
- Fuente, A., Martin-Pintado, J., Bachiller, R., Neri, R., & Palla, F. 1998a, *A&A*, 334, 253
- Fuente, A., Martin-Pintado, J., Bachiller, R., Rodriguez-Franco, A., & Palla, F. 2002, *A&A*, 387, 977
- Fuente, A., Martin-Pintado, J., Rodriguez-Franco, A., & Moriarty-Schieven, G. D. 1998b, *A&A*, 339, 575
- Goldreich, P. & Kwan, J. 1974, *ApJ*, 189, 441
- Goldsmith, P. F. & Langer, W. D. 1999, *ApJ*, 517, 209
- Graves, J. E., Northcott, M. J., Roddier, F. J., Roddier, C. A., & Close, L. M. 1998, in Presented at the Society of Photo-Optical Instrumentation Engineers (SPIE) Conference, Vol. 3353, *Proc. SPIE Vol. 3353*, p. 34–43, Adaptive Optical System Technologies, Domenico Bonaccini; Robert K. Tyson; Eds., ed. D. Bonaccini & R. K. Tyson, 34–43
- Herbig, G. H. 1960, *ApJS*, 4, 337
- Hillenbrand, L. A. 1995, PhD thesis, University of Massachusetts Amherst, Department of Physics and Astronomy
- Hillenbrand, L. A., Strom, S. E., Vrba, F. J., & Keene, J. 1992, *ApJ*, 397, 613
- Lada, C. J. & Lada, E. A. 2003, *ARA&A*, 41, 57
- Larson, R. B. 1979, *MNRAS*, 186, 479
- . 1981, *MNRAS*, 194, 809
- Levreault, R. M. 1988, *ApJS*, 67, 283
- Looney, L. W., Mundy, L. G., & Welch, W. J. 2000, *ApJ*, 529, 477
- . 2003, *ApJ*, 592, 255

- Looney, L. W., Wang, S., Hamidouche, M., Safier, P. N., & Klein, R. 2006, *ApJ*, 642, 330
- Lynds, B. T. 1962, *ApJS*, 7, 1
- Mac Low, M.-M. & Klessen, R. S. 2004, *Reviews of Modern Physics*, 76, 125
- Miao, Y., Mehringer, D. M., Kuan, Y.-J., & Snyder, L. E. 1995, *ApJ*, 445, L59
- Poetzel, R., Mundt, R., & Ray, T. P. 1992, *A&A*, 262, 229
- Ridge, N. A., Wilson, T. L., Megeath, S. T., Allen, L. E., & Myers, P. C. 2003, *AJ*, 126, 286
- Rohlfs, K. & Wilson, T. L. 2000, *Tools of radio astronomy* (Tools of radio astronomy / K. Rohlfs, T.L. Wilson. New York : Springer, 2000. (Astronomy and astrophysics library,ISSN0941-7834))
- Saito, H., Saito, M., Moriguchi, Y., & Fukui, Y. 2006, *PASJ*, 58, 343
- Sault, R. J., Teuben, P. J., & Wright, M. C. H. 1995, in *Astronomical Society of the Pacific Conference Series*, Vol. 77, *Astronomical Data Analysis Software and Systems IV*, ed. R. A. Shaw, H. E. Payne, & J. J. E. Hayes, 433–+
- Shu, F., Najita, J., Galli, D., Ostriker, E., & Lizano, S. 1993, in *Protostars and Planets III*, ed. E. H. Levy & J. I. Lunine, 3–45
- Shu, F. H. 1977, *ApJ*, 214, 488
- Tassis, K. & Mouschovias, T. C. 2005, *ApJ*, 618, 769
- Tobin, J. J., Looney, L. W., Mundy, L. G., Kwon, W., & Hamidouche, M. 2007, *ApJ*, 659, 1404
- Wang, S. & Looney, L. W. 2007, *ApJ*, 659, 1360
- Waters, L. B. F. M. & Waelkens, C. 1998, *ARA&A*, 36, 233
- Welch, W. J., Thornton, D. D., Plambeck, R. L., Wright, M. C. H., Lugten, J., Urry, L., Fleming, M., Hoffman, W., Hudson, J., Lum, W. T., Forster, J. . R., Thatte, N., Zhang, X., Zivanovic, S., Snyder, L., Crutcher, R., Lo, K. Y., Wakker, B., Stupar, M., Sault, R., Miao, Y., Rao, R., Wan, K., Dickel, H. R., Blitz, L., Vogel, S. N., Mundy, L., Erickson, W., Teuben, P. J., Morgan, J., Helfer, T., Looney, L., de Gues, E., Grossman, A., Howe, J. E., Pound, M., & Regan, M. 1996, *PASP*, 108, 93
- Williams, J. P., de Geus, E. J., & Blitz, L. 1994, *ApJ*, 428, 693

Wu, Y., Zhang, Q., Chen, H., Yang, C., Wei, Y., & Ho, P. T. P. 2005, *AJ*, 129, 330

Yoshida, S., Kogure, T., Nakano, M., Tatematsu, K., & Wiramihardja, S. D. 1991, *PASJ*, 43, 363

—. 1992, *PASJ*, 44, 77

Zinnecker, H. & Yorke, H. W. 2007, *ArXiv e-prints*, 707

Table 1. Parameters of Identified CS Clumps

Label	RA. (J2000)	Dec. (J2000)	a_o "	b_o "	PA_o degree	a "	b "	PA degree	R_{eq} 10^{-2} pc	ε
A1	23:17:26.17	60:50:38.12	6.81 ± 0.29	3.60 ± 0.02	-73.65 ± 0.07	5.85	1.33	-73.8	1.49 ± 0.04	0.97 ± 0.04
A2	23:17:26.78	60:50:38.75	11.77 ± 1.37	3.88 ± 0.09	69.30 ± 0.04	11.26	1.85	69.1	2.43 ± 0.16	0.98 ± 0.01
A3	23:17:27.53	60:50:37.43	-	-	-	3.49	3.34	-67.6	1.82	-
A4	23:17:27.59	60:50:44.47	8.11 ± 0.63	6.25 ± 0.41	-36.87 ± 1.91	7.33	5.25	-35.9	3.31 ± 0.19	0.69 ± 0.09
A5	23:17:27.55	60:50:50.40	-	-	-	3.49	3.34	-67.6	1.82	-
A6	23:17:28.11	60:50:51.31	6.75 ± 0.77	4.95 ± 0.13	-11.99 ± 0.82	5.84	3.55	-10.7	2.42 ± 0.16	0.79 ± 0.09
A7	23:17:28.00	60:50:53.19	6.77 ± 3.20	4.63 ± 0.37	-7.57 ± 1.78	5.87	3.08	-6.5	2.27 ± 0.63	0.85 ± 0.30
A8	23:17:28.12	60:50:57.20	6.10 ± 2.24	4.13 ± 0.34	44.68 ± 3.82	5.09	2.24	43.7	1.80 ± 0.42	0.89 ± 0.23
A9	23:17:28.55	60:50:57.32	5.73 ± 0.89	3.31 ± 0.07	-81.44 ± 0.32	3.49	3.34	-67.6	1.82	-
B1	23:17:21.32	60:50:50.99	4.25 ± 0.09	2.74 ± 0.01	-46.23 ± 0.28	3.49	3.34	-67.6	1.82	-
B2	23:17:21.84	60:50:49.41	6.81 ± 3.35	4.49 ± 0.49	87.86 ± 1.67	5.86	2.97	87.0	2.22 ± 0.66	0.86 ± 0.29
B3	23:17:22.72	60:50:49.49	6.95 ± 1.13	4.43 ± 0.17	-82.63 ± 1.17	6.01	2.90	-83.2	2.23 ± 0.22	0.87 ± 0.08
B4	23:17:23.25	60:50:46.58	5.16 ± 0.87	3.35 ± 0.29	78.28 ± 1.41	3.49	3.34	-67.6	1.82	-
B5	23:17:23.32	60:50:52.22	6.23 ± 0.59	4.81 ± 0.22	67.31 ± 2.10	5.21	3.38	65.4	2.24 ± 0.14	0.76 ± 0.09
B6	23:17:24.79	60:50:45.95	6.98 ± 3.60	3.72 ± 0.11	0.47 ± 0.40	6.12	1.33	1.1	1.52 ± 0.45	0.97 ± 0.17
B7	23:17:24.66	60:50:48.18	10.14 ± 3.91	4.98 ± 0.08	-19.60 ± 0.19	9.55	3.62	-19.2	3.13 ± 0.64	0.92 ± 0.10
B8	23:17:24.71	60:50:56.46	4.99 ± 0.26	4.09 ± 0.09	72.30 ± 2.06	3.63	2.25	68.7	1.52 ± 0.06	0.78 ± 0.06
B9	23:17:25.20	60:50:58.36	-	-	-	3.49	3.34	-67.6	1.82	-
B10	23:17:24.58	60:51:02.37	7.89 ± 4.62	4.30 ± 0.26	55.54 ± 1.25	7.13	2.58	54.9	2.28 ± 0.75	0.93 ± 0.20
B11	23:17:24.98	60:51:02.42	7.03 ± 2.73	3.26 ± 0.09	-63.31 ± 0.38	3.49	3.34	-67.6	1.82	-
B12	23:17:24.45	60:51:04.92	4.59 ± 2.18	3.86 ± 0.57	7.20 ± 17.14	3.14	1.66	9.3	1.22 ± 0.47	0.84 ± 0.65
B13	23:17:24.81	60:51:08.29	6.65 ± 3.71	4.29 ± 0.37	26.21 ± 2.56	5.75	2.50	26.1	2.02 ± 0.66	0.90 ± 0.30
B14	23:17:25.15	60:51:10.18	5.24 ± 0.85	3.92 ± 0.41	79.86 ± 2.81	3.95	1.98	77.6	1.49 ± 0.22	0.86 ± 0.16
C1	23:17:27.90	60:50:27.43	-	-	-	3.49	3.34	-67.6	1.82	-
C2	23:17:28.39	60:50:27.61	-	-	-	3.49	3.34	-67.6	1.82	-
C3	23:17:28.06	60:50:23.99	-	-	-	3.49	3.34	-67.6	1.82	-
C4	23:17:27.69	60:50:22.08	-	-	-	3.49	3.34	-67.6	1.82	-
C5	23:17:28.85	60:50:09.20	5.49 ± 0.19	4.01 ± 0.05	-58.20 ± 0.70	4.24	2.22	-57.5	1.63 ± 0.04	0.85 ± 0.02
D1	23:17:21.03	60:50:11.89	5.64 ± 0.71	3.57 ± 0.13	89.11 ± 0.62	4.45	1.21	87.9	1.24 ± 0.12	0.96 ± 0.06
D2	23:17:20.40	60:50:12.78	6.36 ± 0.97	4.76 ± 0.29	-59.04 ± 3.04	5.31	3.38	-58.5	2.26 ± 0.23	0.77 ± 0.13
D3	23:17:27.84	60:51:10.95	5.53 ± 1.67	3.99 ± 0.37	-40.14 ± 5.56	4.31	2.13	-38.4	1.61 ± 0.34	0.86 ± 0.23
D4	23:17:27.60	60:51:12.97	4.57 ± 1.09	3.88 ± 0.55	-43.04 ± 27.76	2.98	1.93	-38.7	1.28 ± 0.29	0.76 ± 0.38

Table 2. Fitted Parameters of CS Integrated Spectra

Label	Peak Jy	Velocity km/s	FWHM km/s
East	4.79 ± 0.31	-31.68 ± 0.06	1.87 ± 0.14
West(N)	3.91 ± 0.37	-30.83 ± 0.08	1.52 ± 0.19
West(S)	1.73 ± 0.25	-34.13 ± 0.26	3.24 ± 0.69

Table 3. Spectral Fitting of CS Clumps

Label	Peak Jy	Velocity km/s	FWHM km/s
A1	0.44 ± 0.05	-31.42 ± 0.07	1.30 ± 0.16
A2	1.77 ± 0.10	-31.70 ± 0.04	1.45 ± 0.09
A3	0.68 ± 0.08	-32.35 ± 0.05	0.85 ± 0.11
A4	1.60 ± 0.09	-31.10 ± 0.05	1.76 ± 0.12
A5	0.45 ± 0.05	-31.37 ± 0.10	1.63 ± 0.23
A6	0.64 ± 0.06	-31.46 ± 0.07	1.52 ± 0.16
A7	0.54 ± 0.05	-31.31 ± 0.08	1.70 ± 0.20
A8	0.20 ± 0.04	-32.33 ± 0.22	2.48 ± 0.52
B2	0.36 ± 0.07	-30.65 ± 0.09	1.00 ± 0.22
B3	0.44 ± 0.08	-30.72 ± 0.13	1.48 ± 0.30
B6	0.50 ± 0.04	-30.92 ± 0.06	1.55 ± 0.14
B7	0.68 ± 0.06	-30.95 ± 0.08	1.84 ± 0.18
C1	0.28 ± 0.04	-30.81 ± 0.13	1.76 ± 0.31
C5	0.35 ± 0.05	-30.73 ± 0.14	1.91 ± 0.33

Table 4. Parameters of the Observed Molecular Lines

Molecular Name	Transition	ν GHz	$S\mu^2$ Debye	Q	E_u K
CS	J = 2 - 1	97.980968	7.71	0.86 T_{ex} ^a	7.0
¹³ CO	J = 1 - 0	110.201370	0.01	0.36 T_{ex}	5.3
C ¹⁸ O	J = 1 - 0	109.782182	0.01	0.36 T_{ex}	5.3

^a T_{ex} is the line excitation temperature.

References. — Rohlfs & Wilson (2000)

Table 5. Mass Estimation of CS Clumps

Label	I_t Jy beam ⁻¹ km s ⁻¹	τ	M_{LTE} M_\odot	$N_{lv}(CS)$ 10^{13} cm ⁻²	M_{LVG} M_\odot	M_{vir} M_\odot
A1	1.755	0.46	3.59	3.43 - 5.56	0.64 - 1.04	2.38
A2	4.210	0.74	9.82	33.93	17.01	4.84
A3	1.631	0.34	3.15	3.64 - 5.91	1.02 - 1.65	1.24
A4	3.832	0.55	8.19	41.18	38.18	9.09
A5	1.557	0.38	3.08	4.30 - 6.98	1.20 - 1.95	4.57
A6	2.649	0.57	5.73	6.51 - 10.56	3.25 - 5.26	5.31
A7	2.582	0.57	5.58	5.71 - 9.28	2.48 - 4.03	6.20
A8	1.328	0.33	2.56	2.48 - 6.55	0.68 - 1.80	10.47
A9	0.930	0.30	1.76	-	-	-
B1	0.572	0.25	1.04	-	-	-
B2	1.042	0.21	1.88	2.07 - 3.36	0.87 - 1.41	2.11
B3	1.399	0.31	2.67	3.91 - 6.33	1.64 - 2.66	4.62
B4	0.799	0.26	1.49	-	-	-
B5	1.266	0.26	2.37	-	-	-
B6	2.012	0.48	4.17	5.21 - 8.46	1.02 - 1.66	3.47
B7	4.457	0.72	10.30	7.88 - 12.79	6.56 - 10.65	10.05
B8	1.582	0.49	3.28	-	-	-
B9	0.950	0.30	1.81	-	-	-
B10	1.516	0.30	2.88	-	-	-
B11	1.031	0.24	1.91	-	-	-
B12	0.703	0.22	1.28	-	-	-
B13	1.102	0.25	2.04	-	-	-
B14	0.810	0.24	1.55	-	-	-
C1	1.103	0.33	2.12	2.85 - 5.91	0.80 - 1.65	5.33
C2	1.444	0.33	2.77	-	-	-
C3	1.600	0.54	3.40	-	-	-
C4	1.200	0.50	2.50	-	-	-
C5	1.059	0.27	1.97	3.95 - 6.42	0.90 - 1.46	5.65

Table 5—Continued

Label	I_t Jy beam ⁻¹ km s ⁻¹	τ	M_{LTE} M_\odot	$N_{lv}(\text{CS})$ 10^{13} cm ⁻²	M_{LVG} M_\odot	M_{vir} M_\odot
D1	0.914	0.23	1.66	-	-	-
D2	1.188	0.24	2.20	-	-	-
D3	0.878	0.24	1.61	-	-	-
D4	0.782	0.26	1.45	-	-	-

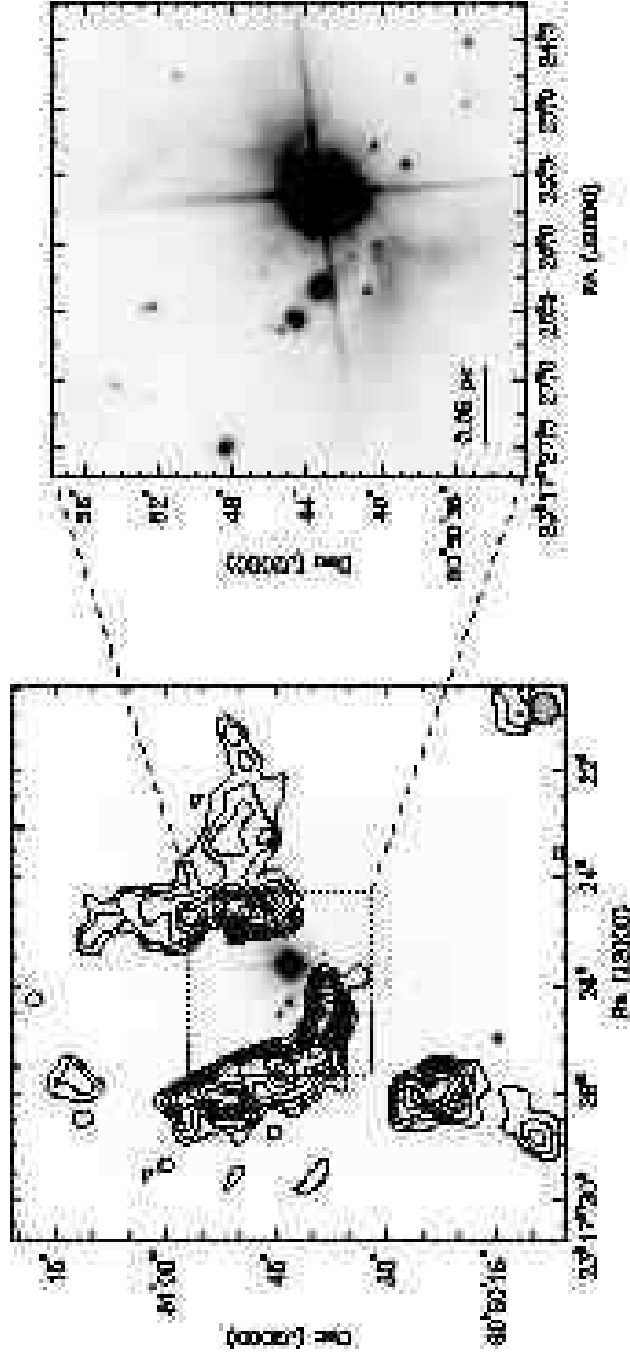


Fig. 1.— Left: CS(2-1) emission toward the MWC 1080 system overlaid on a small adaptive optics K'-band image taken from CFHT (Paper II). The noise is 0.14 Jy/beam km/s. The contours are linearly spaced from 2 to 10 times of noise. The beam, shown at the lower right hand corner, is $4''.04 \times 3''.84$ with a PA of -62° . Negative contours, mainly from resolved out large-scale emission, are not shown here in order to simplify the image. The dotted box indicated the zoomed field of the K'-band image (right) in order to show the distribution of young cluster members more clearly.

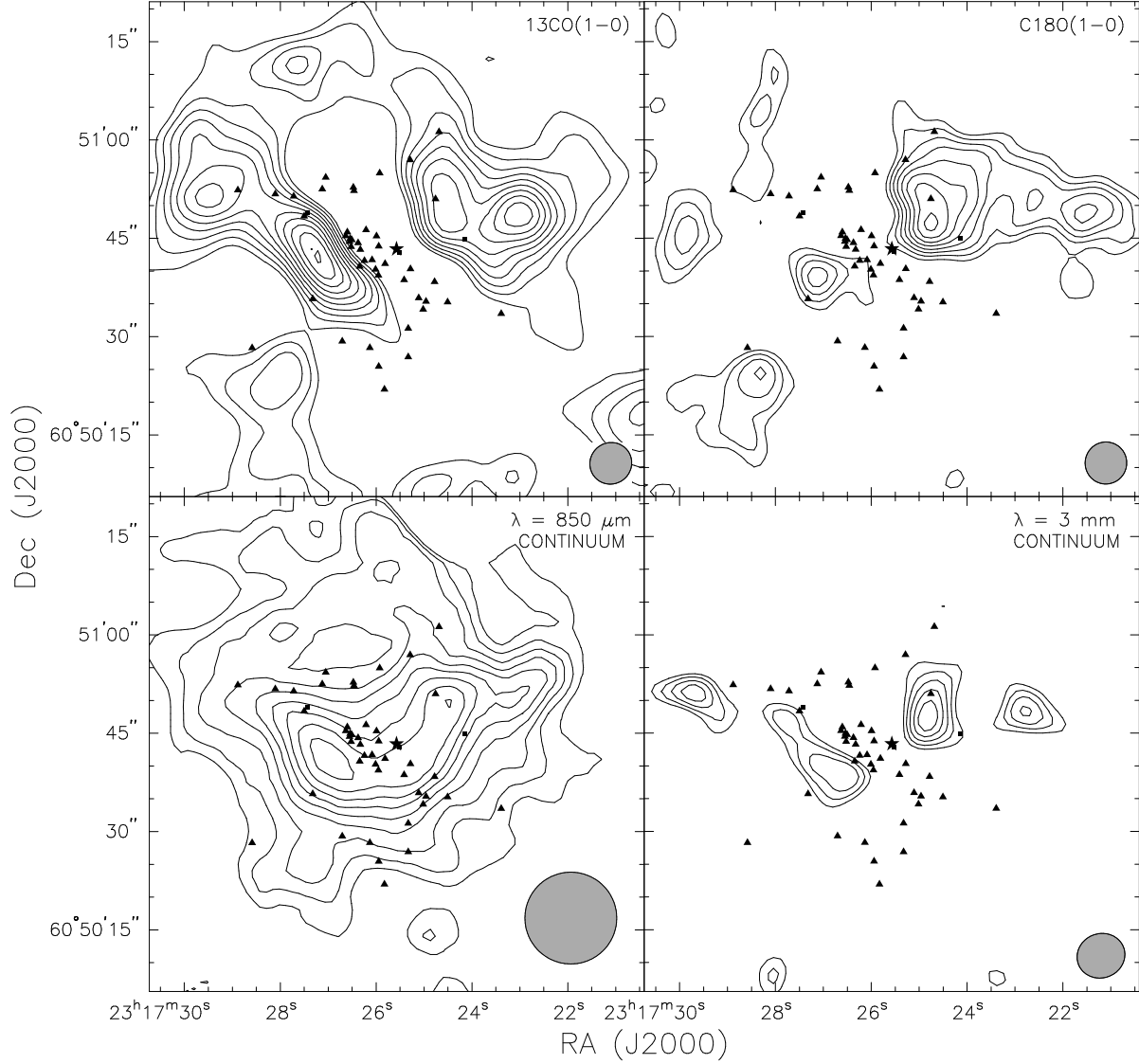


Fig. 2.— ^{13}CO , C^{18}O , and continuum emissions. For ^{13}CO , the noise is 0.3 Jy/beam km/s. The contours are linearly spaced from 2 to 20 times of noise. The beam is $6''.44 \times 6''.28$ with a PA of -51° . For C^{18}O , the noise is 0.12 Jy/beam km/s. The contours are linearly spaced from 2 to 10 times of noise. The beam is $6''.41 \times 6''.34$ with a PA of -13° . For 3 mm continuum map, the noise is 0.009 Jy/beam km/s. The contours are linearly spaced from 2 to 6 times of noise. The beam is $7''.36 \times 6''.74$ with a PA of -70° . Beams are shown at the lower right hand corner of each panel. The star symbols indicate the location of MWC 1080, and the triangle symbols indicate the NIR-identified cluster members from Paper II.

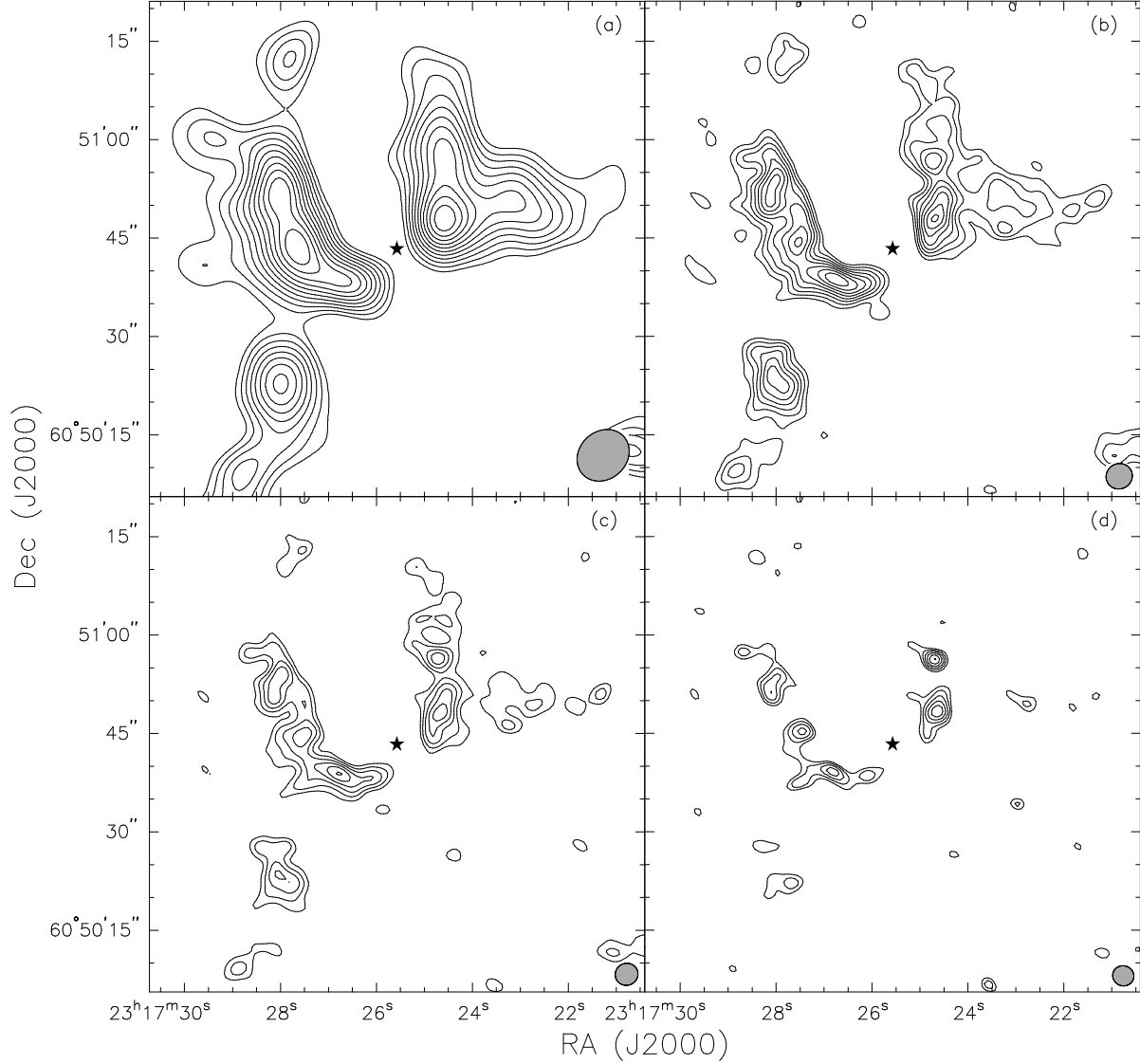


Fig. 3.— The beam sizes are $8''.51 \times 7''.25$ with a PA of -46° , $4''.04 \times 3''.84$ with a PA of -62° , $3''.49 \times 3''.34$ with a PA of -67° , and $3''.24 \times 3''.05$ with a PA of 72° , from (a) to (d) respectively. Beams are shown at the lower right hand corner of each panel. The contours are linearly spaced from (a) 2 to 13 times of noise, 0.23 Jy/beam km/s, (b) 2 to 10 times of noise, 0.14 Jy/beam km/s, (c) 2 to 8 times of noise, 0.16 Jy/beam km/s, (d) 2 to 5 times of noise, 0.25 Jy/beam km/s. The star symbols indicate the location of MWC 1080.

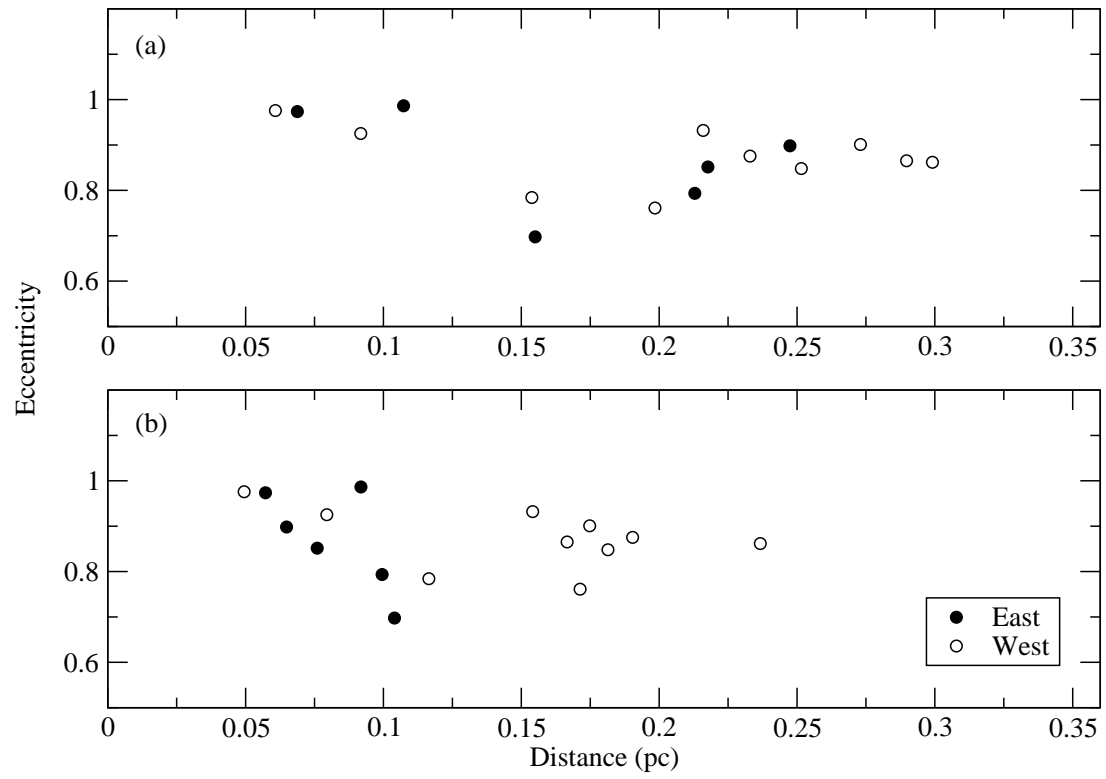


Fig. 4.— The projected eccentricity of clumps vs. the distance to (a) MWC 1080 and (b) outflow axis.

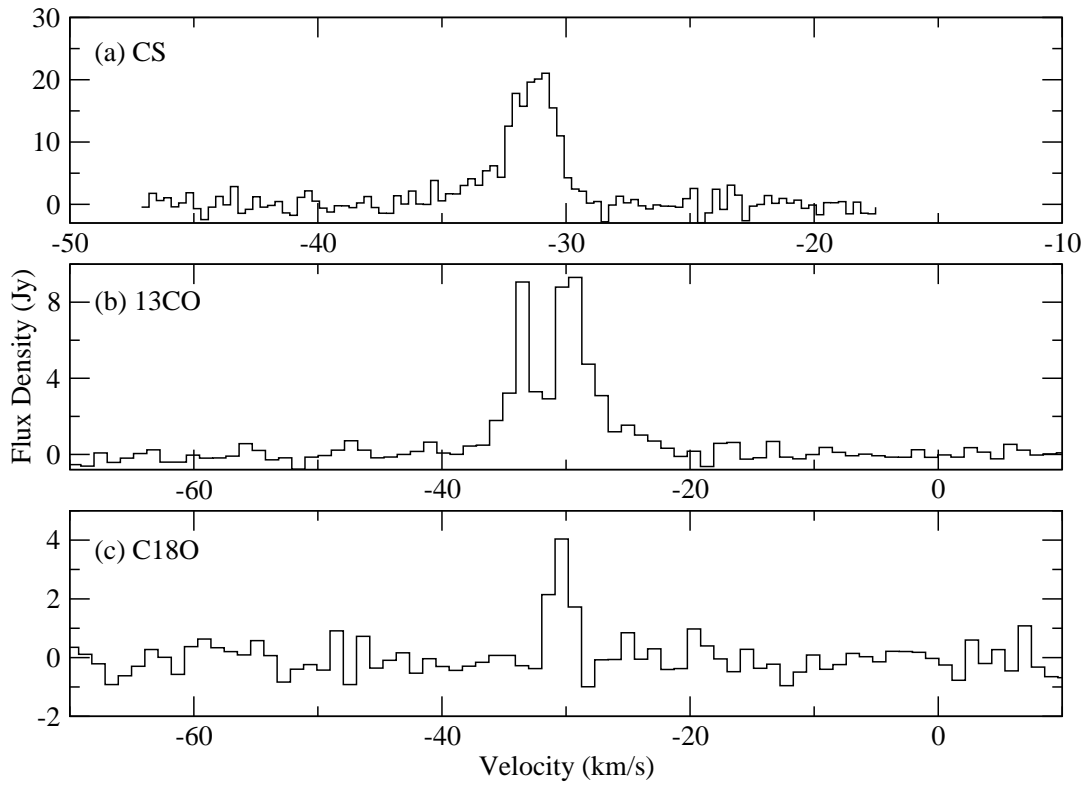


Fig. 5.— Integrated spectra for overall gas traced by CS, ^{13}CO , and C^{18}O .

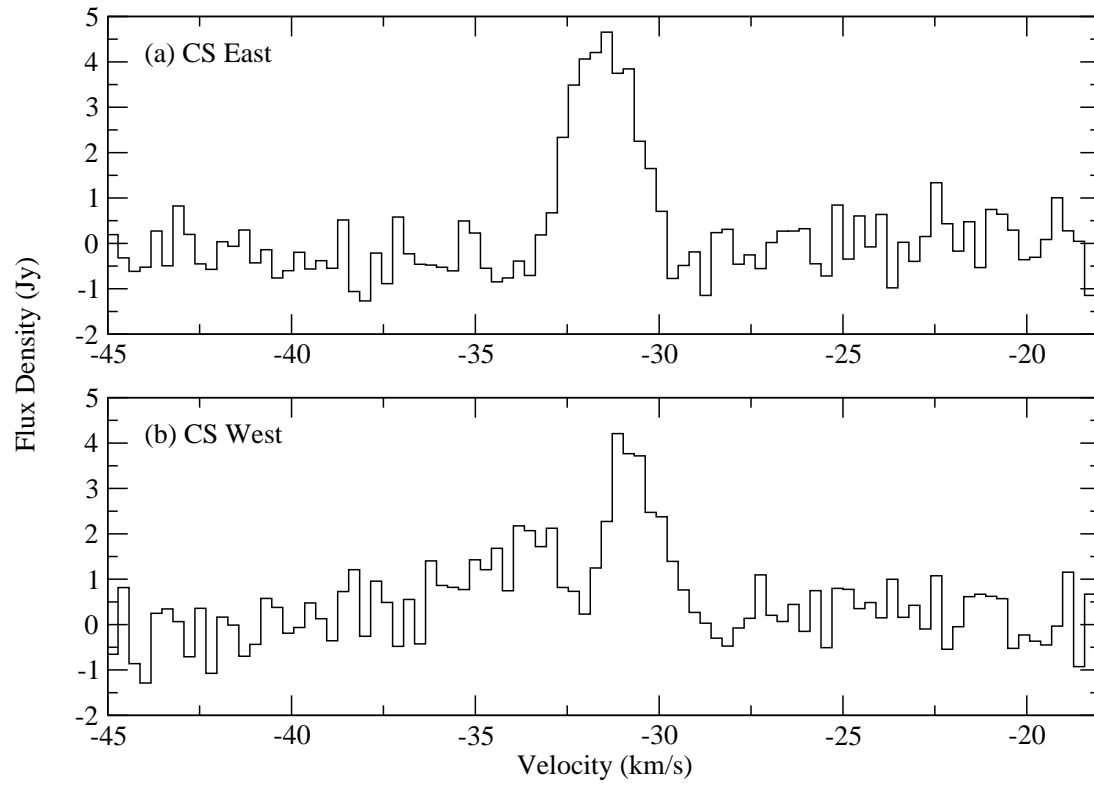


Fig. 6.— Integrated spectra for CS East and West. East shows a broad linewidth; while West shows double-peaked features. This double-peaked feature actually comes from two gas components with different velocities.

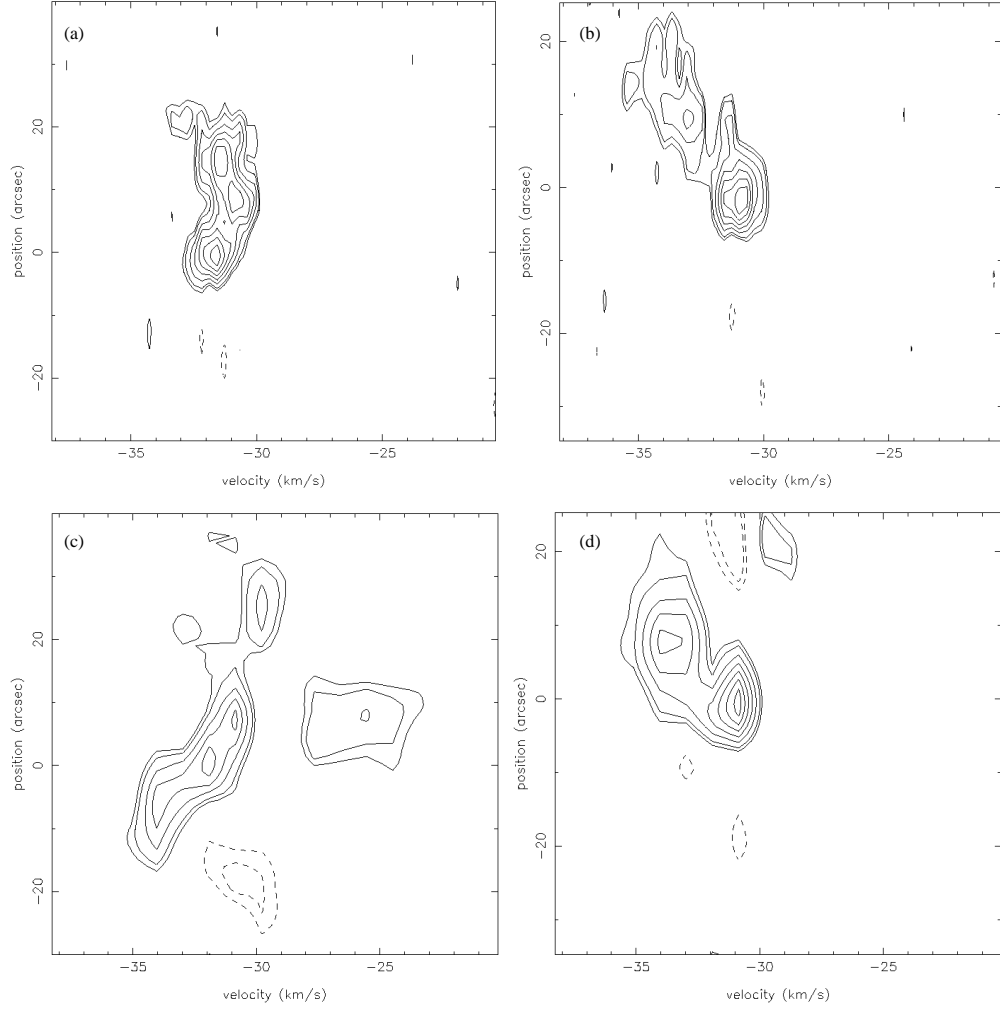


Fig. 7.— Position-velocity (PV) diagrams along the outflow axis for (a) CS East, (b) CS West, (c) ^{13}CO East, and (d) ^{13}CO West. Contours are plotted from 1.5σ , 2σ , 3σ to maximum, with $\sigma = 0.1 \text{ Jy beam}^{-1}$.

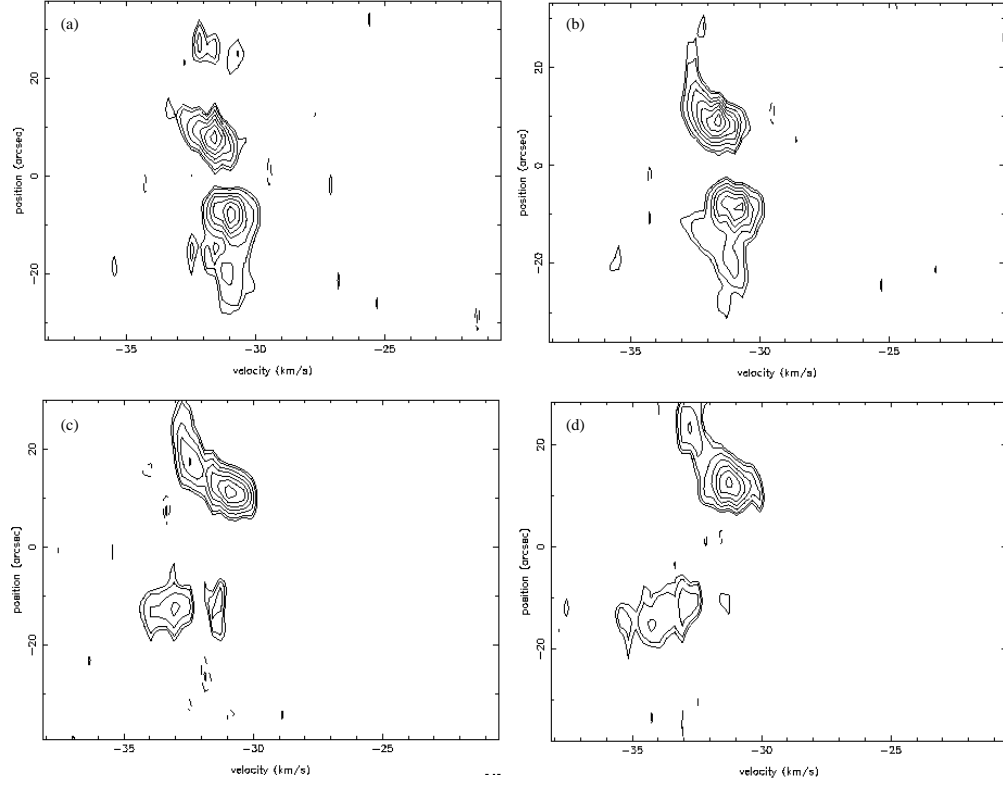


Fig. 8.— PV diagrams along the hourglass axis from closer to MWC 1080 (a) to farther to MWC 1080 (d). Contours are plotted from 1.5σ , 2σ , 3σ to maximum, with $\sigma = 0.1 \text{ Jy beam}^{-1}$.

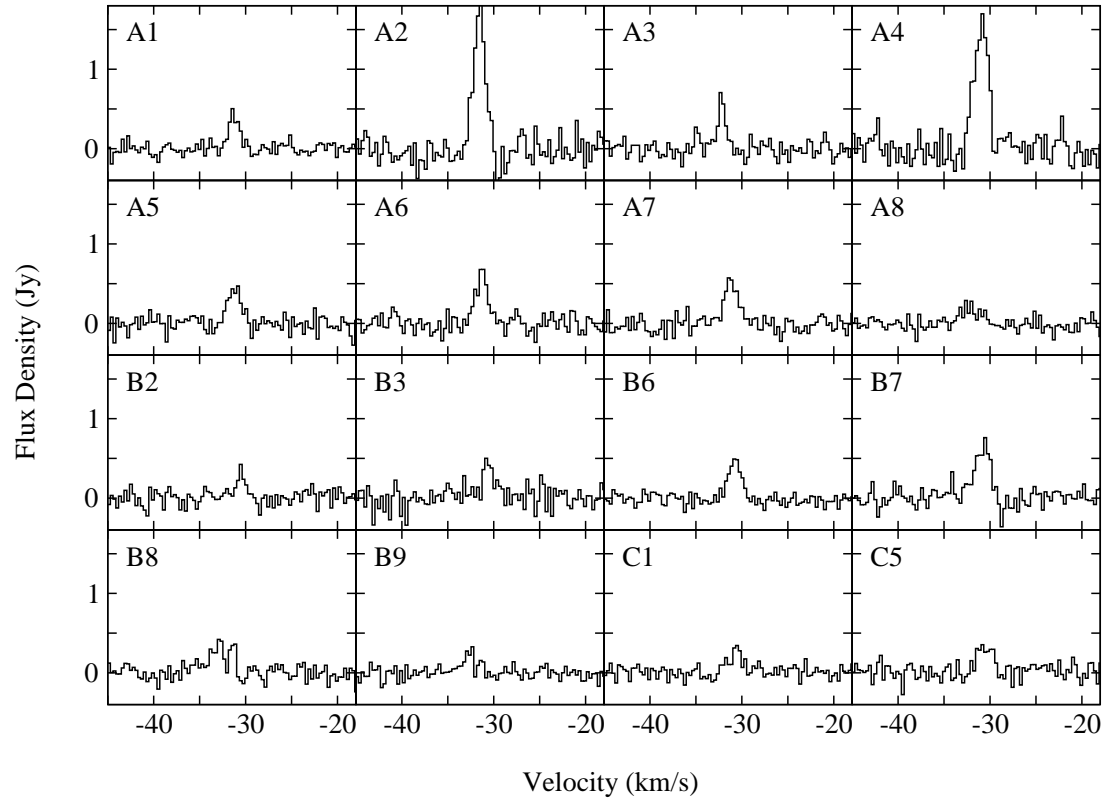
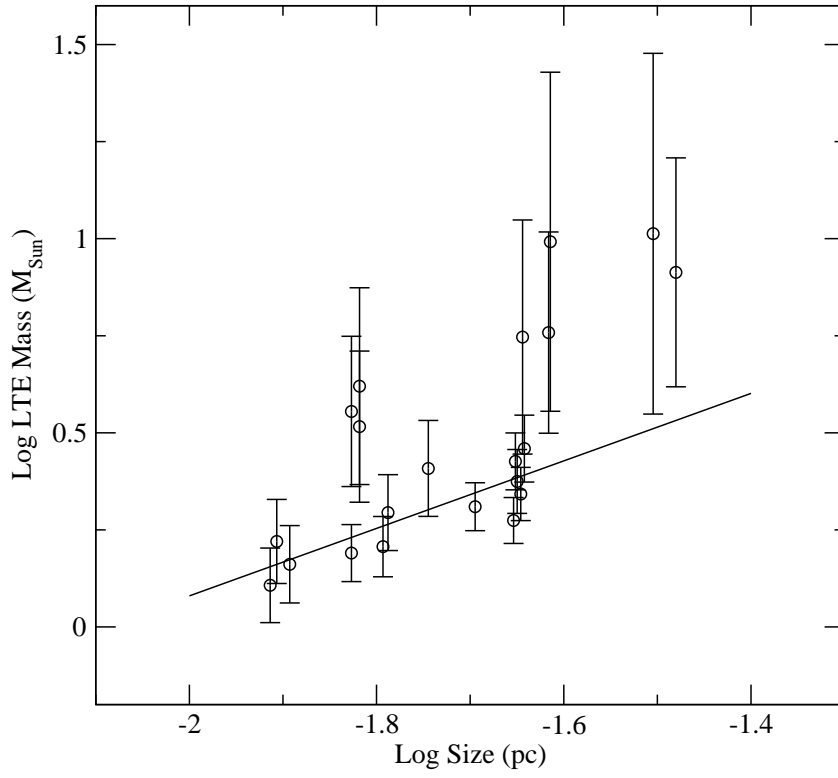


Fig. 9.— Integrated CS spectra for identified CS clumps.



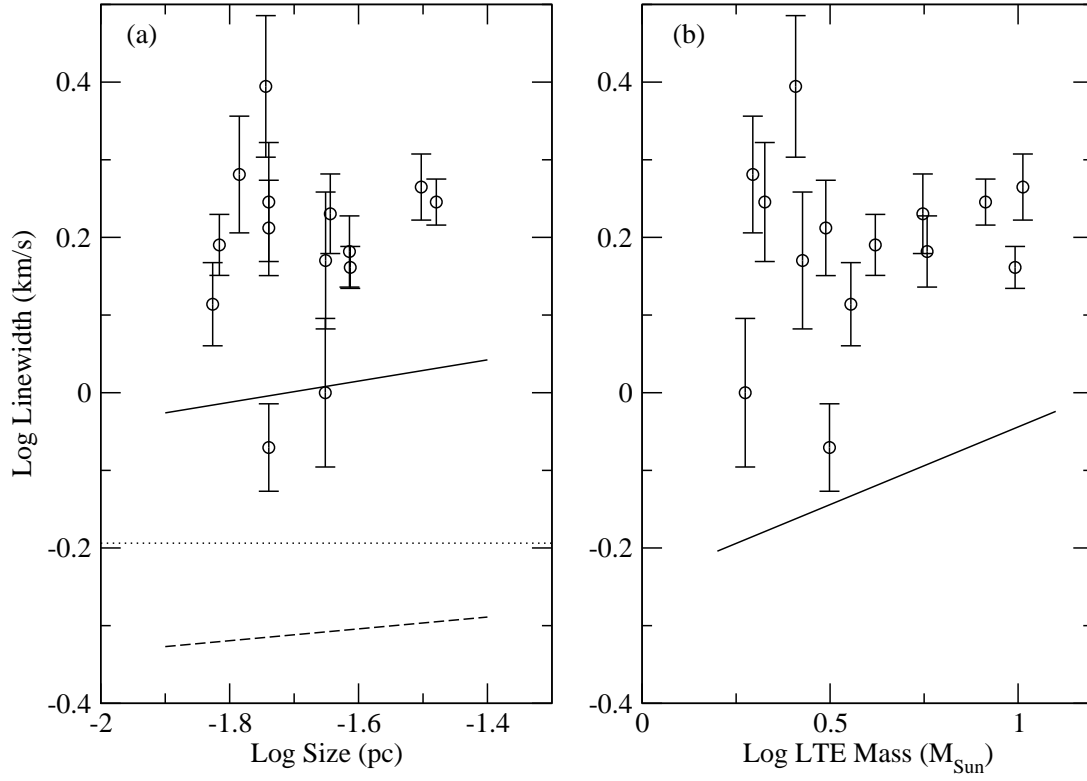


Fig. 11.— The relationship between linewidth vs. (a) size and (b) LTE mass of CS clumps. The solid and dashed lines in (a) indicate the massive cores and low-mass cores (Caselli & Myers 1995), respectively, and the dotted line is the thermal motion at temperature of 20 K. The solid line in (b) indicates the mass-linewidth relation from Larson (1981).

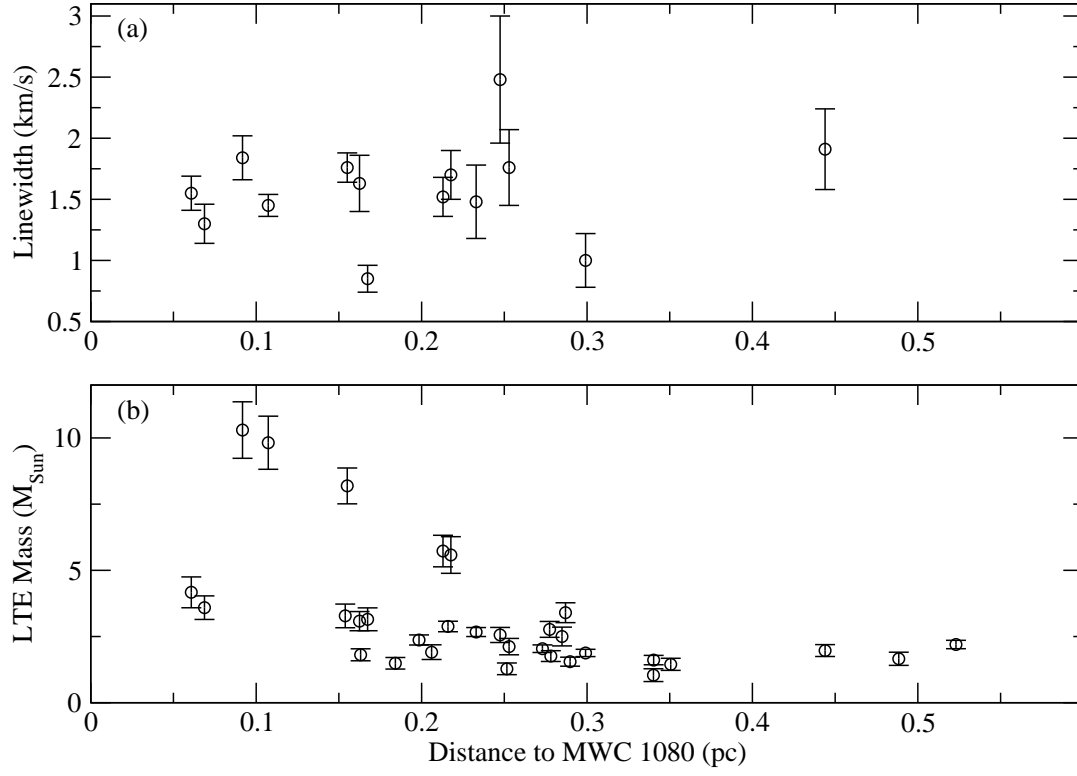


Fig. 12.— (a) The CS linewidth and (b) the derived LTE mass vs. the distance to MWC 1080.

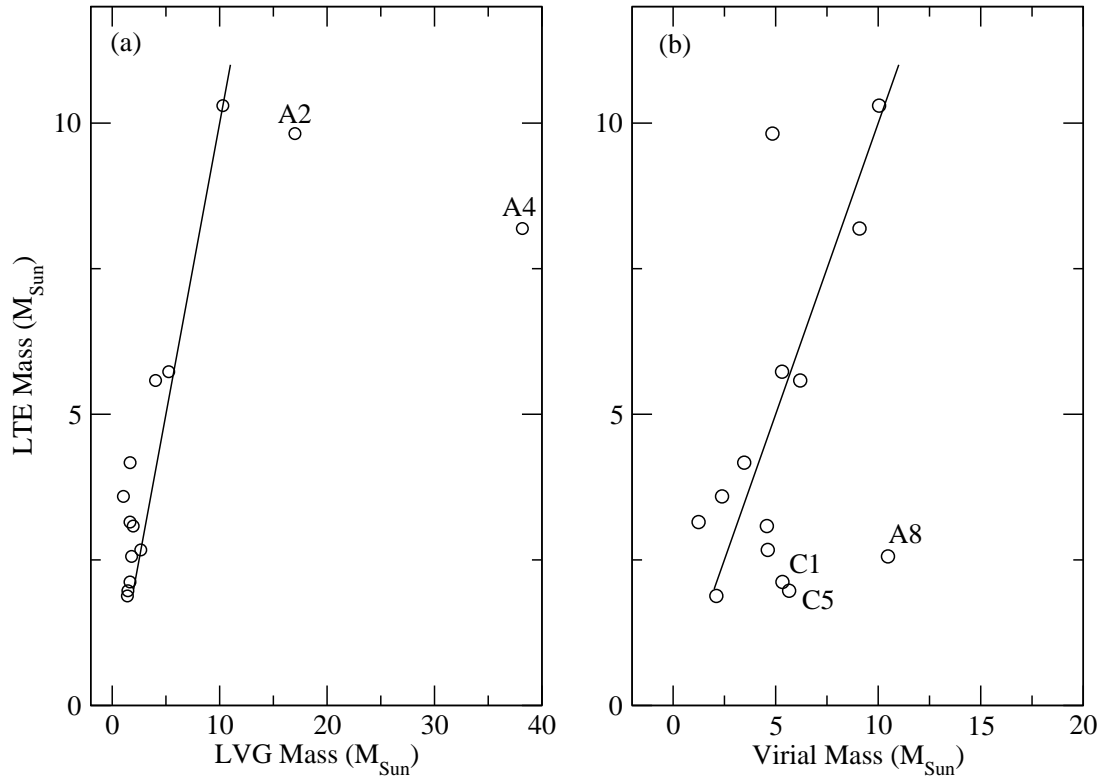


Fig. 13.— The comparison between differently derived masses. The solid lines are when the two masses are equal.